Nonradiative Energy Transfer and Selective Charge Transfer in a WS2/(PEA)2PbI4Heterostructure

Karpińska, Miriam; Liang, Minpeng; Kempt, Roman; Finzel, Kati; Kamminga, Machteld; Dyksik, Mateusz; Zhang, Nan; Knodlseder, Catherine; Maude, Duncan K.; Baranowski, Michał

Published in:
ACS Applied Materials and Interfaces

DOI:
10.1021/acsami.1c08377

ACS APPLIED MATERIALS & INTERFACES

www.acsami.org Research Article

Nonradiative Energy Transfer and Selective Charge Transfer in a $WS_2/(PEA)_2PbI_4$ Heterostructure

Miriam Karpińska, Minpeng Liang, Roman Kempt, Kati Finzel, Machteld Kamminga, Mateusz Dyksik, Nan Zhang, Catherine Knodlseder, Duncan K. Maude, Michał Baranowski, Łukasz Kłopotowski, Jianting Ye, Agnieszka Kuc,* and Paulina Plochocka*

Cite This: *ACS Appl. Mater. Interfaces* 2021, 13, 33677−33684 Read Online

ACCESS | Metrics & More | Article Recommendations | Supporting Information

ABSTRACT: van der Waals heterostructures are currently the focus of intense investigation; this is essentially due to the unprecedented flexibility offered by the total relaxation of lattice matching requirements and their new and exotic properties compared to the individual layers. Here, we investigate the hybrid transition-metal dichalcogenide/2D perovskite heterostructure $WS_2/(PEA)_2PbI_4$ (where PEA stands for phenylethylammonium). We present the first density functional theory (DFT) calculations of a heterostructure ensemble, which reveal a novel band alignment, where direct electron transfer is blocked by the organic spacer of the 2D perovskite. In contrast, the valence band forms a cascade from WS_2 through the PEA to the PbI_4 layer allowing hole transfer. These predictions are supported by optical spectroscopy studies, which provide compelling evidence for both charge transfer and nonradiative transfer of the excitation (energy transfer) between the layers. Our results show that TMD/2D perovskite (where TMD stands for transition-metal dichalcogenides) heterostructures provide a flexible and convenient way to engineer the band alignment.

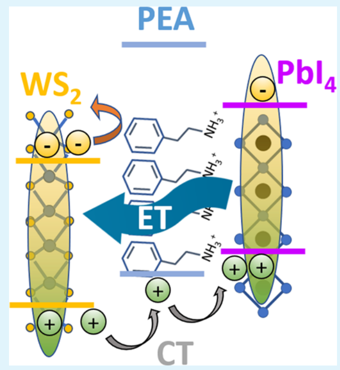

KEYWORDS: *TMDs, 2D perovskites, WS_2, heterostructure, charge transfer, energy transfer, photoluminescence*

■ INTRODUCTION

Two-dimensional (2D) layered materials have been in the scientific spotlight for more than a decade.[1,2] The seminal work of Geim and Novosolov on graphene[3,4] was followed by the rediscovery of transition-metal dichalcogenides (TMDs),[5,6] the recent explosion of the field of 2D perovskites,[7,8] and other emerging layered materials.[9,10] While initially the investigations of electronic properties were limited to monolayers within a particular group of materials, recently, the engineering of van der Waals stacks has attracted tremendous attention.[11−15] The inherently weak van der Waals interaction between the 2D crystals facilitates the stacking of a variety of different layers into hetero- or homostructures[16] with new functional properties. The encapsulation of TMDs with h-BN results in superior electrical and optical quality. Stacking two different TMDs leads to a plethora of new properties, including long-lived interlayer excitons,[17] which can be controlled by an electric or magnetic field,[18−20] and the formation of a moiré pattern,[21,22] which can lead to exotic crystal phases.[12,23]

These functional properties strongly depend on the nature of the spatial excitation transfer between the layers, which can rely on charge transfer and/or energy transfer. For example, the type-II band alignment in TMD stacks[24] favors charge transfer, which leads to the formation of interlayer excitons with new exotic properties.[12,21,22,25] On the other hand, stacks of 2D semiconductors, in principle, form an ideal platform to explore energy transfer (nonradiative transfer of the excitation). This is due to the large oscillator strength and ultimate proximity of the functional layers (in the range of single to a few dozens of Å), essential for nonradiative energy transfer of the Förster or Dexter type.[26−31] The energy transfer can be the dominant process if the direct interlayer charge transfer is strongly suppressed. This can be achieved, for example, by separating TMD layers with an insulating sheet of h-BN.[31,32] The incorporation of different numbers of h-BN layers allows us to control the mechanism of excitation transfer from a direct charge transfer to an energy transfer.[31−34]

Here, we propose a novel approach to control the excitation transfer process, using a hybrid heterostructure built from a TMD monolayer and a 2D perovskite $(PEA)_2PbI_4$ (PEPI),[7] which is presented schematically in Figure 1a. The 2D perovskite provides a charge blocking layer in the form of organic spacers. As we show here, such a stack can provide a rather unique band alignment, not achievable in TMD-based van der Waals heterostructures. Taking into account the plethora of available organic spacers that can be incorporated

Received: May 6, 2021
Accepted: June 17, 2021
Published: July 6, 2021

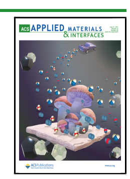

https://doi.org/10.1021/acsami.1c08377
ACS Appl. Mater. Interfaces 2021, 13, 33677−33684

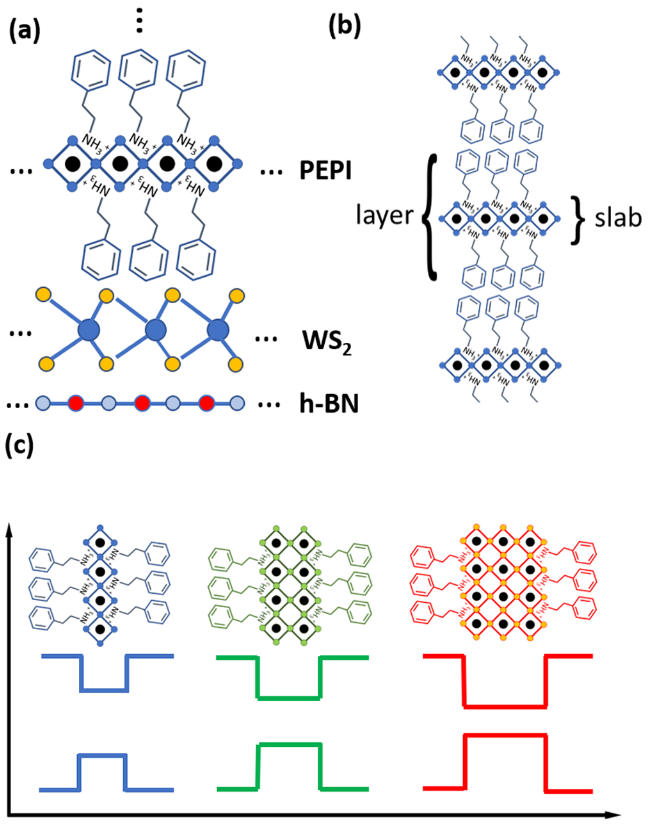

Figure 1. (a) Schematic of the investigated structure. On an h-BN layer, a monolayer of WS_2 is deposited, followed by a multilayer of $(PEA)_2PbI_4$ (PEPI), which is encapsulated by a top layer h-BN (not shown). (b) Schematic of the 2D perovskite structure with a single slab of inorganic octahedral units PbI_6 separated by organic spacers. (c) Schematic of the type-I band alignment of the perovskite with different thicknesses of the inorganic layers.

into the 2D perovskites,[7] this new approach to heterostructure design provides greater flexibility in the band alignment, together with the possibility to engineer the excitation transfer mechanism. The efficient energy transfer can be used to sensitize the photoresponse of one layer (for example, TMD) using the other layer (2D perovskite), without reduction of the overall photoresponse yield characteristic for the interlayer charge transfer and weak interlayer emission.

Two-dimensional Ruddlesden−Popper-type organic−inorganic perovskites consist of inorganic metal-halide octahedral slabs separated by large organic molecules (see Figure 1a). They can be regarded as ideal quantum wells due to the lack of interface roughness and usually exhibit type-I band alignment (Figure 1c), which prevents efficient charge transfer between the neighboring slabs.[7,8] The thickness of the inorganic slab determines the optical band gap of such 2D perovskites, and can thus be used to sensitize TMDs monolayers to different photon energies. Interestingly, the character of the band gap does not depend on the slab thickness or the number of layers,[35] in contrast to the case of TMDs.[5] At the same time, 2D perovskites suffer from poor electrical properties (carrier mobility μ in the range of single $cm^2\ V^{-1}\ s^{-1}$) and TMDs are far better (2−3 orders of magnitude higher) in this respect.[36,37] Therefore, an appropriate utilization of charge or energy transfer can serve to suppress the drawbacks of individual layers, while enhancing their advantages, allowing, for example, the creation of efficient photodetectors.[38−40]

However, despite the potential advantages and recent very interesting results[38−40] showing high sensing potential of such heterostructures, very little is known about their fundamental properties, in particular, the excitation transfer mechanism. The understanding of the mutual relation between band alignment of the individual layer and the excitation transfer mechanism is crucial for the future deterministic design of these devices. The few works addressing these aspects are far from conclusive.[41−43] They point to energy transfer,[41] charge

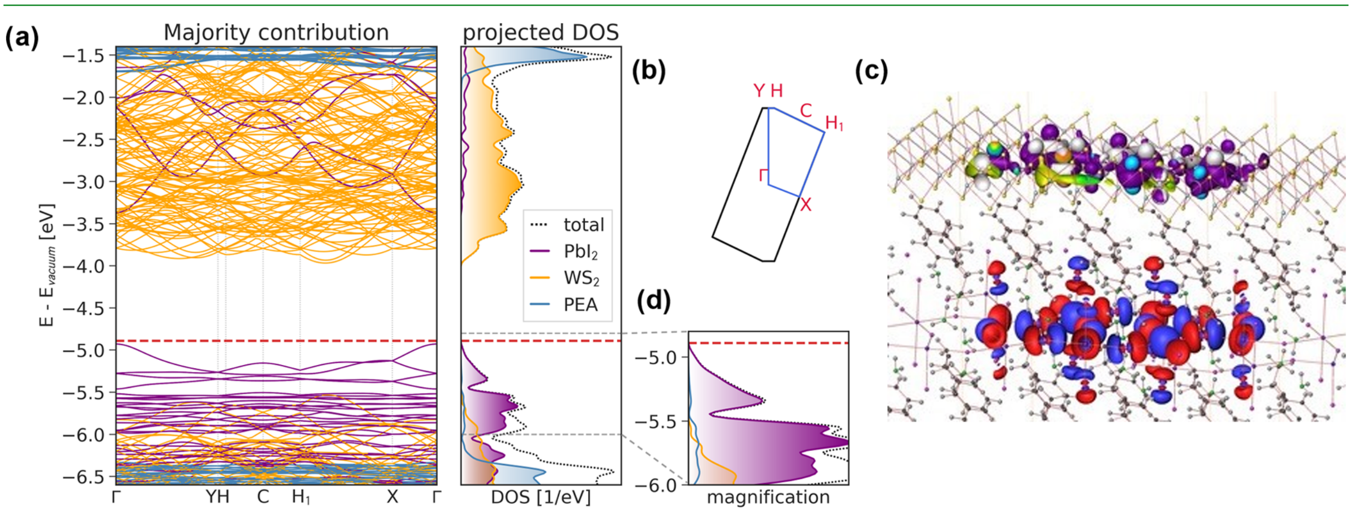

Figure 2. (a) Mulliken-projected band structure of the WS_2/PEPI heterostructure showing the majority contributions of each layer and density of states projected to particular building blocks (WS_2, PEA, PbI_4). (b) The corresponding Brillouin zone and k-path of this low-symmetry model structure. Both band structure and density of states indicate type-II band alignment, which is also visible in the real-space representation of the highest occupied and lowest unoccupied crystal orbitals from the corresponding *k*-points in the band structure (c). The valence band maximum (VBM) is localized in the PbI_4 layer, while the conduction band minimum (CBM) is localized in the WS_2 layer. The orbitals are depicted using a 0.02 amplitude isosurface. The VBM is located at Γ (0,0,0), and therefore is real-valued; the negative and positive amplitudes are shown in blue and red, respectively. In the case of the complex-valued CBM, located at (0,1,0), the phase is indicated by the color map, ranging from -10^{-17} (violet) to 10^{-17} (white). (d) Magnification of the density of states close to the valance band to show the spurious contribution of organic ligand states.

https://doi.org/10.1021/acsami.1c08377
ACS Appl. Mater. Interfaces 2021, 13, 33677−33684

transfer,[42] and an optically active state at the hybrid interfaces.[43] To date, band alignments were determined from independent calculations of the TMD and perovskite layers[41,44,45] using different methods. Taking into account the accuracy of simulations based on density functional theory (DFT),[46] notably the predicted band gap, it is crucial to calculate the heterostructure as an ensemble to correctly determine the band alignments. Here, we present such DFT calculations. We show that the $(PEA)_2PbI_4/WS_2$ stack possesses a novel band aliment, where only electron transfer between the layers is blocked. This prediction is supported by our experimental results, which point to a hole transfer from the WS_2 to the 2D perovskite, and an energy transfer in the opposite direction. Our results show that such 2D perovskite/TMD hybrid structures can be effectively used to sensitize TMDs to a particular excitation photon energy.

■ RESULTS

We start with the DFT calculations, which are to the best of our knowledge the first theoretical results that take into account the full structure and orbital hybridization of a TMDs/2D perovskite heterostructure. Figure 2a shows the calculated band structure of $WS_2/(PEA)_2PbI_4$ heterostructure (the h-BN encapsulation is neglected in the calculations), where the 2D Brillouin zone of this system is indicated in panel (b) with the sampled reciprocal directions.

The band structure was projected on the majority contribution from the Mulliken analysis. This shows that the top of the valence band is mainly composed of orbitals from the PbI_4 slab, while the conduction band is dominated by the WS_2 states, as clearly seen in the density of states (DOS) plot. Consequently, a type-II band alignment is formed between the WS_2 layer and the PbI_4 slab. Additionally, Figure 2c shows a representation of the real-space highest occupied and lowest unoccupied crystal orbitals, which correspond to the valence band maximum (VBM) and conduction band minimum (CBM). The VBM at Γ is localized mostly in the PbI_4 layer, while the CBM at Ω is localized in the WS_2 layer, in accordance with the calculated DOS.

In the investigated structure, the WS_2 layer is separated from the PbI_4 slab by the wide-band-gap PEA organic spacer. The conduction band alignment provides a barrier for electron transfer between the WS_2 and the PbI_4 layer. Indeed, based on the Hirshfeld charge analysis, we find negligible charge transfer from the WS_2 layer to the organic spacers of $0.1e^-$ averaged over the whole model structure consisting of 239 atoms. Moreover, in the valence band, we have an interesting situation. The peak of the PEA density of states is located around −6.5 eV; however, a closer inspection of the density of states plot (see Figure 2d) reveals that there are also states related to PEA slightly above WS_2 and below PbI_4. In fact, the density of these states is comparable to the WS_2 density of states close to the top of valence band. Therefore, in the valence band, the WS_2, PEA, and PbI_4 band edges form a funnel (cascade), which favors the transfer of photoinduced holes from WS_2 to the PbI_4 layer. Thus, stacking WS_2 with $(PEA)_2PbI_4$ leads to a novel band diagram, presented in Figure 3, where only one type of carrier can be directly transferred between the layers, *i.e.*, holes. At the same time, strong excitonic effects (in the sense of the oscillator strength) in both materials, together with their proximity, should favor energy transfer from the perovskite layer to the TMD layer.

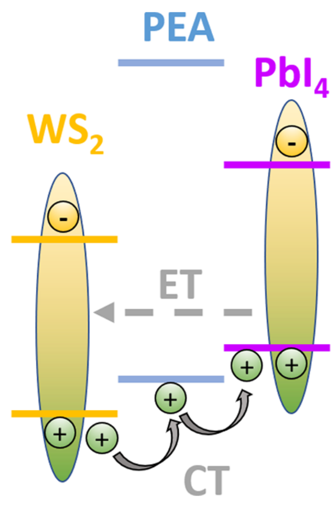

Figure 3. Summary of the band alignment in the $PEPI/WS_2$ heterostructure resulting from DFT calculations. The charge transfer (CT) and energy transfer (ET) paths are indicated.

To corroborate theoretical predictions, we have performed optical studies on the $WS_2/(PEA)_2PbI_4$ stack, which is placed on a Si/SiO_2 substrate, and encapsulated in h-BN to provide the highest possible optical quality and stability. Figure 4a shows the optical microscope image of the sample. Three characteristic regions can be clearly distinguished, namely, the bare Ruddlesden−Popper perovskite $(PEA)_2PbI_4$, bare monolayer WS_2, and the WS_2/PEPI heterostructure area. The perovskite region is roughly 20 × 20 μm^2, and the triangular WS_2 flake also has sides ≃20 μm.

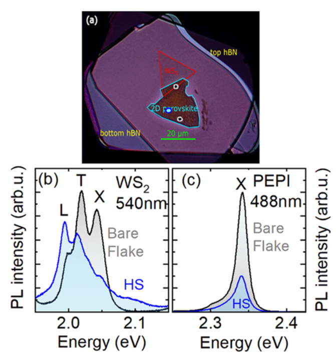

Figure 4. (a) Optical microscope image of WS_2/PEPI heterostructure sandwiched between h-BN capping layers. Color points on the image correspond to spectra shown in the remaining panels. (b) PL spectra of WS_2, excited below (540 nm) the absorption band of PEPI, and (c) PL spectra of $(PEA)_2PbI_4$ (PEPI) excited above (488 nm) the absorption band of PEPI. All spectra are taken at T = 5 K. In panels (b−c), the spectra are taken on the heterostructure (blue) and on the bare flakes (gray).

The optical properties of WS_2 monolayers are characterized by the presence of the A- and B-excitons, which arise from the spin−orbit splitting in the valence band. In emission, generally, only the A-exciton is observed due to the large splitting (≃400meV) of the valence band. Figure 4b shows representative PL spectra, related to the WS_2 emission, taken on the bare flake and in the heterostructure region, measured at T = 5 K. We can distinguish three emission features characteristic for A-exciton emission, which can be attributed to the free exciton (X), trion (T), and localized excitons (L).[47]

https://doi.org/10.1021/acsami.1c08377
ACS Appl. Mater. Interfaces 2021, 13, 33677−33684

Even though the PL from WS_2 was collected using 540 nm excitation in Figure 4b (*i.e.*, below the absorption band of PEPI), the spectra of bare WS_2 flake and the heterostructure are different. The trion-to-exciton ratio is changed from ≃1.2 on the bare flake to ≃2 on the heterostructure. In addition, the overall intensity of the WS_2 trion and exciton emission from the heterostructure is lower than on the bare flake. This finding supports the theoretically predicted hole transfer from the WS_2 layer to the PbI_4 slab. The efficient hole transfer reduces the overall PL intensity in the heterostructure region. Moreover, as the WS_2 layer is intrinsically n-type,[48,49] the trion is negatively charged. The increase of the T/X emission ratio in the heterostructure indicates an increased ratio of the electron/hole concentration, which is a result of the photoinduced hole transfer from WS_2 to the PEPI layer.

When the sample is excited above the absorption band of PEPI (488 nm laser), strong PL emission is observed around 2.34 eV corresponding to the dominant free exciton emission of PEPI[50−52] (Figure 4c). The PEPI PL signal from the isolated flake is more intense than in the heterostructure region. However, taking into account predicted band alignment, the lower intensity in the heterostructure region cannot result from a direct charge/exciton transfer to the WS_2 layer. This suggests that the reduced PL intensity is an indication of an energy transfer process from PEPI to the WS_2 layer. However, just from the PL measurement with a single excitation wavelength of 488 nm, it is hard to conclude if the WS_2 emission in the heterostructure area is enhanced (as expected in the case of an energy transfer from PEPI). The PL emission from WS_2 overlaps with the bound-state emission from PEPI (see Figure S1), which is visible everywhere on the PEPI flake (see Figure S2). Therefore, we perform photoluminescence excitation (PLE) at 5 K studies, which provide further evidence of an energy transfer process from PEPI to WS_2. We varied the excitation photon energy in the range 2.3−2.6 eV while monitoring the emission intensity of the WS_2 exciton and trion recombination. The result of this experiment is shown in Figure 5. The PLE emission from the bare WS_2 flake (gray symbols) is slightly enhanced when the excitation is resonant with the B-exciton of WS_2, due to the increased absorption.[53] The moderate increase of intensity, going to lower energies, observed below 2.4 eV, corresponds to the approaching resonant A-exciton absorption in monolayer WS_2. Crucially, for PLE in the heterostructure region, an extra feature appears at ≃2.37 eV, *i.e.*, at an energy corresponding to the ground-state exciton absorption in PEPI, also seen in the reflectivity spectrum (black line). The increased PL intensity, when exciting resonantly the exciton transition in PEPI, is roughly the same for the trion and exciton PL from the WS_2 monolayer. This shows that the charge state of the WS_2 monolayer does not change when exciting via the PEPI. We, therefore, exclude the presence of a charge transfer process within the heterostructure under resonant excitation conditions and conclude that an energy transfer process is responsible for the increased excitation efficiency (increased PL intensity). This energy transfer process involves the exciton ground state in PEPI and an electron-hole continuum state in monolayer WS_2.

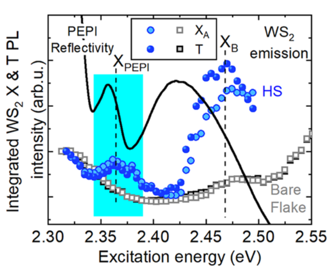

Figure 5. PL integrated intensity of X_A and T from WS_2 as a function of excitation energy in heterostructure region (blue) and on the bare flake (gray) together with reflection spectrum from PEPI (black). The excitonic resonance feature visible in reflectance spectrum corresponds to PLE feature. The reflection spectrum overlaps with interference pattern resulting from h-BN encapsulation. All spectra taken at T = 5 K.

An additional indication of energy transfer is the strongly increased exciton and trion emission when exciting resonantly the B-exciton of WS_2 at ≃2.47eV. Indeed, if no energy transfer occurred, the exciton and trion PL intensity in the heterostructure region would be the same as for the isolated monolayer. Increased PL intensity indicates another energy transfer process involving the B-exciton in monolayer WS_2 and probably excited exciton states (2s, 3s,...) in PEPI.[54−56] The large enhancement in the WS_2 exciton and trion PL intensity in Figure 5 shows that this energy transfer process is more efficient than the energy transfer when exciting the PEPI exciton ground state at 2.37 eV. Since the energy transfer efficiency of a Förster or Dexter type is proportional to the product of the oscillator strengths of the energy donor and acceptor, our results suggest that this product is significantly larger for PEPI excited excitons states and the WS_2 B-exciton than for WS_2 free carriers and PEPI 1s state. Overall, the results presented in Figure 5 show an efficient sensitization of the WS_2 monolayer via energy transfer from PEPI.

It is interesting to note that the particular situation of hole transfer from WS_2 to PEPI is possible only for monolayer WS_2. For bilayer and above, the energy of the valance band edge is pushed up at the Γ point, making WS_2 indirect.[57] This will suppress hole transfer between the TMD and the 2D perovskite due to the faster intralayer hole relaxation (to Γ point of the thicker WS_2) compared to the interlayer transfer. At the same time, the energy transfer should still be possible because the energy of the bands at the *K*-points of TMDs are only weakly affected by the thickness. Such a configuration is potentially beneficial for sensing applications, where the excitation transferred to TMDs is not lost due to hole transfer or radiative emission in indirect-band-gap semiconductors so that the excitation is more effectively converted to current.

Finally, we consider the nature of the energy transfer process. In the heterostructure, the centers of the WS_2 and PbI_4 layers are separated by about 1−1.5 nm. This distance is often considered as limiting for Dexter-type processes, but not for Förster.[26−31,58,59] Moreover, the Dexter-type mechanism involves an exchange of carriers between states. Hence, in addition to an overlap of the emission and absorption energies, the Dexter mechanism requires an overlap of the wavefunctions of the donor and acceptor states. As the DFT calculations show that the wavefunction overlap is negligible, we conclude that the Förster process is the most probable mechanism for the energy transfer.

CONCLUSIONS

We have presented the evidence for both charge and energy transfer in the $(PEA)_2PbI_4/WS_2$ heterostructure at low temperatures. Due to particular band alignment between the

https://doi.org/10.1021/acsami.1c08377
ACS Appl. Mater. Interfaces 2021, 13, 33677−33684

PEPI and WS_2 layers, only the hole transfer is present from the TMD to the 2D perovskite. Simultaneously, the electron exchange between the layer is completely blocked. However, the excitation can be transferred from $(PEA)_2PbI_4$ to WS_2 via an energy transfer process, which is especially efficient close to the B-exciton resonance in WS_2. This is confirmed by PLE studies showing that WS_2 monolayer can be effectively sensitized by the $(PEA)_2PbI_4$ 2D perovskite.

METHODS

Synthesis and Sample Preparation. The device has a multilayer structure composed of a boron nitride (h-BN) top layer (∼100 nm), a WS_2 monolayer, a $(PEA)_2PbI_4$ perovskite (≃50nm), and an h-BN bottom layer (≃120nm). The WS_2 monolayer is grown by the chemical vapor deposition.[60] Both $(PEA)_2PbI_4$ perovskite and boron nitride flakes are exfoliated from their bulk crystals. Single crystals of $(PEA)_2PbI_4$ were grown at room temperature using the same layered solution crystal growth technique as used in our previous work.[61] To avoid the degradation of $(PEA)_2PbI_4$ perovskite under the ambient condition, cleavage, transfer, and stacking are all carried out in an argon-filled glovebox with a trace amount of H_2O and O_2 (both less than 0.1 ppm). During the transfer process, the top h-BN layer is picked up by a polycarbonate film (PC) at 80 °C, and then WS_2 monolayer and $(PEA)_2PbI_4$ perovskite flakes are picked up by the top h-BN layer at 110 and 40 °C, respectively. Care was taken to minimize the heating process to avoid the thermal degradation of the perovskite. The PC on the sandwiched structure is then quickly dissolved in chloroform within 3 min. We have confirmed that the optical properties of the perovskite are not affected by the solution process after being sandwiched between WS_2 and h-BN. Additional optical and PL images of the sample can be seen in the Supporting Information (Figures S4−S6). The thickness of each flake was estimated as follows: For WS2, we used the optical image, PL, AFM, and Raman to characterize the thickness of the flake. All techniques confirm it is a monolayer. For the hBN, since different thicknesses will induce different reflection/absorption wavelengths, we estimated the thickness from its color in the optical image. We have checked hBN flakes with same color before, and the thickness of hBN was more than 100 nm. For the 2D perovskite, we estimated the thickness from optical contrast, estimating it to be around 50nm. The perovskite layers degrade in air, preventing us from performing AFM measurements.

DFT Calculations. A bilayer model structure of WS_2@$(PEA)_2PbI_4$ was created in the Virtual NanoLab[62] with less than 0.1% strain on the individual layers, resulting in a superstructure with 239 atoms. For such a strain, the overall change in the band gap is less than a few millielectron volts[63−65] and therefore cannot affect the conclusions of our work.

The structure can be represented by supercell vectors $m_1 = (-3, -2)$, $m_2 = (4,2)$, $n_1 = (-3,8)$, and $n_2 = (2,-11)$ with a rotation angle of $\theta = 79.00°$ and a vacuum spacing of 100 Å (see ref 66 for details (other representation choices are possible)). This model structure was relaxed using FHI aims[67] employing the PBE functional[68] on tight tier 1 numeric atom-centered orbitals, including the nonlocal many-body dispersion correction (MBD-nl)[69,70] and scalar relativistic corrections (ZORA) on a $4 \times 4 \times 1$ Γ-centered k-grid. The γ-angle was kept fixed, while forces and stresses were minimized till below 0.05 eV $Å^{-1}$. The SCF parameters were adjusted automatically after four steps. The electronic band structure, the Mulliken projections, and the density of states were calculated including spin−orbit coupling (SOC) and considering the dipole correction on a $6 \times 6 \times 1$ Γ-centered k-grid.

Optical Measurements. The sample was mounted on the cold finger of a liquid helium-cooled cryostat. Both reflectivity and PL measurements were performed on the home-built setup at the temperature of around 5 K. The excitation source was a halogen lamp (for reflectivity) and a continuous-wave 488 nm gas laser or second harmonic of a Ti:sapphire laser (for PL). The white light/laser beam was focused on the sample by a 50× microscope objective with a numerical aperture of 0.55, resulting in a spot size of ≃1 μm. The signal from the sample was collected by the same objective, directed to the 0.5 m long monochromator and detected by a liquid nitrogen-cooled CCD camera. For PL, the laser beam was filtered out by the long-pass 488 or 550 nm edge filter. Spatial PL maps with the step of 1 μm along the x and y axes were possible with the use of an automated xy translation stages on which the cryostat was mounted. PLE experiments were performed using the same setup as the PL measurements at 5 K. The excitation source was the second harmonic of a Ti:sapphire laser with a repetition rate of 80 MHz and a temporal pulse width of 300 fs. The laser signal was filtered out by the 550 nm long-pass edge filter before entering the monochromator and CCD camera.

ASSOCIATED CONTENT

Supporting Information

The Supporting Information is available free of charge at https://pubs.acs.org/doi/10.1021/acsami.1c08377.

PL spectra taken of bare WS_2 flake and the PEPI/WS_2 heterostructure with excitation 488 nm, spatial PL intensity map of bound exciton peak of PEPI, trion-to-exciton PL intensity ratio, and optical images of heterostructure just after stacking procedure (PDF)

AUTHOR INFORMATION

Corresponding Authors

Agnieszka Kuc − *Helmholtz-Zentrum Dresden-Rossendorf, 01328 Dresden, Germany*; orcid.org/0000-0002-9458-4136; Email: a.kuc@hzdr.de

Paulina Plochocka − *Laboratoire National des Champs Magnétiques Intenses, UPR 3228, CNRS-UGA-UPS-INSA, 31400 Toulouse, France; Department of Experimental Physics, Faculty of Fundamental Problems of Technology, Wroclaw University of Science and Technology, 50-370 Wroclaw, Poland*; orcid.org/0000-0002-4019-6138; Email: paulina.plochocka@lncmi.cnrs.fr

Authors

Miriam Karpińska − *Laboratoire National des Champs Magnétiques Intenses, UPR 3228, CNRS-UGA-UPS-INSA, 31400 Toulouse, France; Institute of Physics, Polish Academy of Sciences, 02-668 Warsaw, Poland*

Minpeng Liang − *Zernike Institute for Advanced Materials, University of Groningen, 9747 AG Groningen, The Netherlands*

Roman Kempt − *Technische Universität Dresden, 01062 Dresden, Germany*

Kati Finzel − *Technische Universität Dresden, 01062 Dresden, Germany*; orcid.org/0000-0002-0862-2782

Machteld Kamminga − *Zernike Institute for Advanced Materials, University of Groningen, 9747 AG Groningen, The Netherlands*

Mateusz Dyksik − *Laboratoire National des Champs Magnétiques Intenses, UPR 3228, CNRS-UGA-UPS-INSA, 31400 Toulouse, France; Department of Experimental Physics, Faculty of Fundamental Problems of Technology, Wroclaw University of Science and Technology, 50-370 Wroclaw, Poland*; orcid.org/0000-0003-4945-8795

Nan Zhang − *Laboratoire National des Champs Magnétiques Intenses, UPR 3228, CNRS-UGA-UPS-INSA, 31400 Toulouse, France*; orcid.org/0000-0003-4269-6811

Catherine Knodlseder − *Laboratoire National des Champs Magnétiques Intenses, UPR 3228, CNRS-UGA-UPS-INSA, 31400 Toulouse, France*

https://doi.org/10.1021/acsami.1c08377
ACS Appl. Mater. Interfaces 2021, 13, 33677−33684

Duncan K. Maude − *Laboratoire National des Champs Magnétiques Intenses, UPR 3228, CNRS-UGA-UPS-INSA, 31400 Toulouse, France*

Michał Baranowski − *Department of Experimental Physics, Faculty of Fundamental Problems of Technology, Wroclaw University of Science and Technology, 50-370 Wroclaw, Poland*; orcid.org/0000-0002-5974-0850

Łukasz Kłopotowski − *Institute of Physics, Polish Academy of Sciences, 02-668 Warsaw, Poland*; orcid.org/0000-0001-8327-2156

Jianting Ye − *Zernike Institute for Advanced Materials, University of Groningen, 9747 AG Groningen, The Netherlands*

Complete contact information is available at: https://pubs.acs.org/10.1021/acsami.1c08377

Notes

The authors declare no competing financial interest.

■ ACKNOWLEDGMENTS

M.E.K. was supported by The Netherlands Organization for Scientific Research (NWO Graduate Programme 2013, No. 022.005.006). P.P. appreciates support from National Science Centre Poland within the OPUS program (grant no. 2019/33/B/ST3/01915). This work was partially supported by OPEP project, which received funding from the ANR-10-LABX-0037-NEXT. This is a publication of the FOM-focus Group "Next Generation Organic Photovoltaics," financed by the Netherlands Organization for Scientific Research (NWO) and participating in the Dutch Institute for Fundamental Energy Research (DIFFER). S.A. acknowledges the financial support of the Netherlands Organization for Scientific Research (NWO graduate project 2013, No 022.005.006). The Polish participation in European Magnetic Field Laboratory is supported by the DIR/WK/2018/07 grant from Ministry of Science and Higher Education, Poland. A.K., R.K., and K.F. gratefully acknowledge the Gauss Centre for Supercomputing e.V. (www.gauss-centre.eu for funding this project by providing computing time through the John von Neumann Institute for Computing (NIC) on the GCS Supercomputer JUWELS at Jülich Supercomputing Centre (JSC). Furthermore, A.K., R.K., and K.F. gratefully acknowledge the support from GWK for funding this project by providing computing time through the Center for Information Services and HPC (ZIH) at TU Dresden. A.K. acknowledges the financial support from Deutsche Forschungsgemeinschaft (DFG, German Research Foundation) within SFB1415 project number 417590517 and the association with the SPP2244 (2DMP).

■ REFERENCES

(1) Tan, C.; Cao, X.; Wu, X.-J.; He, Q.; Yang, J.; Zhang, X.; Chen, J.; Zhao, W.; Han, S.; Nam, G.-H.; Sindoro, M.; Zhang, H. Recent Advances in Ultrathin Two-dimensional Nanomaterials. *Chem. Rev.* **2017**, *117*, 6225−6331.
(2) Geng, D.; Yang, H. Y. Recent Advances in Growth of Novel 2d Materials: Beyond Graphene and Transition Metal Dichalcogenides. *Adv. Mater.* **2018**, *30*, No. 1800865.
(3) Novoselov, K. S.; Geim, A. K.; Morozov, S. V.; Jiang, D.; Zhang, Y.; Dubonos, S. V.; Grigorieva, I. V.; Firsov, A. A. Electric Field Effect in Atomically Thin Carbon Films. *Science* **2004**, *306*, 666−669.
(4) Geim, A. K. Nobel Lecture: Random Walk to Graphene. *Rev. Mod. Phys.* **2011**, *83*, 851.
(5) Mak, K. F.; Lee, C.; Hone, J.; Shan, J.; Heinz, T. F. Atomically Thin Mos 2: A New Direct-gap Semiconductor. *Phys. Rev. Lett.* **2010**, *105*, No. 136805.
(6) Xu, X.; Yao, W.; Xiao, D.; Heinz, T. F. Spin and Pseudospins in Layered Transition Metal Dichalcogenides. *Nat. Phys.* **2014**, *10*, 343−350.
(7) Chen, Y.; Sun, Y.; Peng, J.; Tang, J.; Zheng, K.; Liang, Z. 2d Ruddlesden-popper Perovskites for Optoelectronics. *Adv. Mater.* **2018**, *30*, No. 1703487.
(8) Straus, D. B.; Kagan, C. R. Electrons, Excitons, and Phonons in Two-dimensional Hybrid Perovskites: Connecting Structural, Optical, and Electronic Properties. *J. Phys. Chem. Lett.* **2018**, *9*, 1434−1447.
(9) Castellanos-Gomez, A.; Vicarelli, L.; Prada, E.; Island, J. O.; Narasimha-Acharya, K. L.; Blanter, S. I.; Groenendijk, D. J.; Buscema, M.; Steele, G. A.; Alvarez, J. V.; Zandbergen, H. W.; Palacios, J. J.; van der Zant, H. S. J. Isolation and Characterization of Few-layer Black Phosphorus. *2D Mater.* **2014**, *1*, No. 025001.
(10) Gibertini, M.; Koperski, M.; Morpurgo, A.; Novoselov, K. Magnetic 2d Materials and Heterostructures. *Nat. Nanotechnol.* **2019**, *14*, 408−419.
(11) Liu, Y.; Weiss, N. O.; Duan, X.; Cheng, H.-C.; Huang, Y.; Duan, X. van der Waals Heterostructures and Devices. *Nat. Rev. Mater.* **2016**, *1*, No. 16042.
(12) Tang, Y.; Li, L.; Li, T.; Xu, Y.; Liu, S.; Barmak, K.; Watanabe, K.; Taniguchi, T.; MacDonald, A. H.; Shan, J.; Mak, K. F. Simulation of Hubbard Model Physics in Wse 2/ws 2 Moiré Superlattices. *Nature* **2020**, *579*, 353−358.
(13) Geim, A. K.; Grigorieva, I. V. van der Waals Heterostructures. *Nature* **2013**, *499*, 419−425.
(14) Yu, H.; Liu, G.-B.; Tang, J.; Xu, X.; Yao, W. Moiré Excitons: From Programmable Quantum Emitter Arrays to Spin-orbit-coupled Artificial Lattices. *Sci. Adv.* **2017**, *3*, No. e1701696.
(15) Zhang, N.; Surrente, A.; Baranowski, M.; Maude, D. K.; Gant, P.; Castellanos-Gomez, A.; Plochocka, P. Moiré Intralayer Excitons in a Mose2/mos2 Heterostructure. *Nano Lett.* **2018**, *18*, 7651−7657.
(16) Scuri, G.; Andersen, T.; Zhou, Y.; Wild, D.; Sung, J.; Gelly, R.; Bérubé, D.; Heo, H.; Shao, L.; Joe, A.; Valdivia, A. M. M.; Taniguchi, T.; Watanabe, K.; Lončar, M.; Kim, P.; Lukin, M.; Park, H. Electrically Tunable Valley Dynamics in Twisted WSe2/WSe2 Bilayers. *Phys. Rev. Lett.* **2020**, *124*, No. 217403.
(17) Rivera, P.; Schaibley, J. R.; Jones, A. M.; Ross, J. S.; Wu, S.; Aivazian, G.; Klement, P.; Seyler, K.; Clark, G.; Ghimire, N. J.; Yan, J.; Mandrus, D. G.; Yao, W.; Xu, X. Observation of Long-lived Interlayer Excitons in Monolayer Mose 2-wse 2 Heterostructures. *Nat. Commun.* **2015**, *6*, No. 6242.
(18) Surrente, A.; Kłopotowski, Ł.; Zhang, N.; Baranowski, M.; Mitioglu, A. A.; Ballottin, M. V.; Christianen, P. C.; Dumcenco, D.; Kung, Y.-C.; Maude, D. K.; Kis, A.; Plochocka, P. Intervalley Scattering of Interlayer Excitons in a Mos2/mose2/mos2 Heterostructure in High Magnetic Field. *Nano Lett.* **2018**, *18*, 3994−4000.
(19) Ciarrocchi, A.; Unuchek, D.; Avsar, A.; Watanabe, K.; Taniguchi, T.; Kis, A. Polarization Switching and Electrical Control of Interlayer Excitons in Two-dimensional van der Waals Heterostructures. *Nat. Photonics* **2019**, *13*, 131−136.
(20) Nagler, P.; Ballottin, M. V.; Mitioglu, A. A.; Mooshammer, F.; Paradiso, N.; Strunk, C.; Huber, R.; Chernikov, A.; Christianen, P. C.; Schüller, C.; Korn, T. Giant Magnetic Splitting Inducing Near-unity Valley Polarization in van der Waals Heterostructures. *Nat. Commun.* **2017**, *8*, No. 1551.
(21) Seyler, K. L.; Rivera, P.; Yu, H.; Wilson, N. P.; Ray, E. L.; Mandrus, D. G.; Yan, J.; Yao, W.; Xu, X. Signatures of Moiré-trapped Valley Excitons in Mose 2/wse 2 Heterobilayers. *Nature* **2019**, *567*, 66−70.
(22) Tran, K.; Moody, G.; Wu, F.; Lu, X.; Choi, J.; Kim, K.; Rai, A.; Sanchez, D. A.; Quan, J.; Singh, A.; Embley, J.; Zepeda, A.; Campbell, M.; Autry, T.; Taniguchi, T.; Watanabe, K.; Lu, N.; Banerjee, S. K.; Silverman, K. L.; Kim, S.; Tutuc, E.; Yang, L.; MacDonald, A. H.; Li, X. Evidence for Moiré Excitons in van der Waals Heterostructures. *Nature* **2019**, *567*, 71−75.

(23) Regan, E. C.; Wang, D.; Jin, C.; Utama, M. I. B.; Gao, B.; Wei, X.; Zhao, S.; Zhao, W.; Zhang, Z.; Yumigeta, K.; Blei, M.; Carlström, J. D.; Watanabe, K.; Taniguchi, T.; Tongay, S.; Crommie, M.; Zettl, A.; Wang, F. Mott and Generalized Wigner Crystal States in Wse 2/ws 2 Moiré Superlattices. *Nature* **2020**, *579*, 359−363.
(24) Gong, C.; Zhang, H.; Wang, W.; Colombo, L.; Wallace, R. M.; Cho, K. Band Alignment of Two-dimensional Transition Metal Dichalcogenides: Application in Tunnel Field Effect Transistors. *Appl. Phys. Lett.* **2013**, *103*, No. 053513.
(25) Jin, C.; Regan, E. C.; Yan, A.; Utama, M. I. B.; Wang, D.; Zhao, S.; Qin, Y.; Yang, S.; Zheng, Z.; Shi, S.; Watanabe, K.; Taniguchi, T.; Tongay, S.; Zettl, A.; Wang, F. Observation of Moiré Excitons in Wse 2/ws 2 Heterostructure Superlattices. *Nature* **2019**, *567*, 76−80.
(26) Förster, T. 10th Spiers Memorial Lecture. Transfer Mechanisms of Electronic Excitation. *Discuss. Faraday Soc.* **1959**, *27*, 7−17.
(27) Dexter, D. L. A Theory of Sensitized Luminescence in Solids. *J. Chem. Phys.* **1953**, *21*, 836−850.
(28) Becker, K.; Lupton, J. M.; Müller, J.; Rogach, A. L.; Talapin, D. V.; Weller, H.; Feldmann, J. Electrical Control of Förster Energy Transfer. *Nat. Mater.* **2006**, *5*, 777−781.
(29) Lyo, S. K. Energy Transfer of Excitons between Quantum Wells Separated by a Wide Barrier. *Phys. Rev. B: Condens. Matter Mater. Phys.* **2000**, *62*, 13641−13656.
(30) Kozawa, D.; Carvalho, A.; Verzhbitskiy, I.; Giustiniano, F.; Miyauchi, Y.; Mouri, S.; Neto, A. H. C.; Matsuda, K.; Eda, G. Evidence for Fast Interlayer Energy Transfer in MoSe2/WS2 Heterostructures. *Nano Lett.* **2016**, *16*, 4087−4093.
(31) Hu, Z.; Hernández-Martínez, P. L.; Liu, X.; Amara, M.-R.; Zhao, W.; Watanabe, K.; Taniguchi, T.; Demir, H. V.; Xiong, Q. Trion-mediated Förster Resonance Energy Transfer and Optical Gating Effect in WS2/hBN/MoSe2 Heterojunction. *ACS Nano* **2020**, *14*, 13470−13477.
(32) Liu, X.; Pei, J.; Hu, Z.; Zhao, W.; Liu, S.; Amara, M.-R.; Watanabe, K.; Taniguchi, T.; Zhang, H.; Xiong, Q. Manipulating Charge and Energy Transfer between 2d Atomic Layers Via Heterostructure Engineering. *Nano Lett.* **2020**, *20*, 5359−5366.
(33) Zhang, L.; Sharma, A.; Zhu, Y.; Zhang, Y.; Wang, B.; Dong, M.; Nguyen, H. T.; Wang, Z.; Wen, B.; Cao, Y.; Liu, B.; Sun, X.; Yang, J.; Li, Z.; Kar, A.; Shi, Y.; Macdonald, D.; Yu, Z.; Wang, X.; Lu, Y. Efficient and Layer-dependent Exciton Pumping across Atomically Thin Organic-inorganic Type-i Heterostructures. *Adv. Mater.* **2018**, *30*, No. 1803986.
(34) Xu, W.; Kozawa, D.; Liu, Y.; Sheng, Y.; Wei, K.; Koman, V. B.; Wang, S.; Wang, X.; Jiang, T.; Strano, M. S.; Warner, J. H. Determining the Optimized Interlayer Separation Distance in Vertical Stacked 2d Ws2: Hbn: Mos2 Heterostructures for Exciton Energy Transfer. *Small* **2018**, *14*, No. 1703727.
(35) Blancon, J.-C.; Stier, A. V.; Tsai, H.; Nie, W.; Stoumpos, C. C.; Traoré, B.; Pedesseau, L.; Kepenekian, M.; Katsutani, F.; Noe, G. T.; Kono, J.; Tretiak, S.; Crooker, S. A.; Katan, C.; Kanatzidis, M. G.; Crochet, J. J.; Even, J.; Mohite, A. D. Scaling Law for Excitons in 2d Perovskite Quantum Wells. *Nat. Commun.* **2018**, *9*, No. 2254.
(36) Yu, Z.; Ong, Z.-Y.; Li, S.; Xu, J.-B.; Zhang, G.; Zhang, Y.-W.; Shi, Y.; Wang, X. Analyzing the Carrier Mobility in Transition-metal Dichalcogenide Mos2 Field-effect Transistors. *Adv. Funct. Mater.* **2017**, *27*, No. 1604093.
(37) Fallahazad, B.; Movva, H. C.; Kim, K.; Larentis, S.; Taniguchi, T.; Watanabe, K.; Banerjee, S. K.; Tutuc, E. Shubnikov−de Haas Oscillations of High-mobility Holes in Monolayer and BilayerWSe2: Landau Level Degeneracy, Effective Mass, and Negative Compressibility. *Phys. Rev. Lett.* **2016**, *116*, No. 086601.
(38) Fu, Q.; Wang, X.; Liu, F.; Dong, Y.; Liu, Z.; Zheng, S.; Chaturvedi, A.; Zhou, J.; Hu, P.; Zhu, Z.; Bo, F.; Long, Y.; Liu, Z. Ultrathin Ruddlesden-popper Perovskite Heterojunction for Sensitive Photodetection. *Small* **2019**, *15*, No. 1902890.
(39) Leng, K.; Wang, L.; Shao, Y.; Abdelwahab, I.; Grinblat, G.; Verzhbitskiy, I.; Li, R.; Cai, Y.; Chi, X.; Fu, W.; Song, P.; Rusydi, A.; Eda, G.; Maier, S. A.; Loh, K. P. Electron Tunneling at the Molecularly Thin 2d Perovskite and Graphene van der Waals Interface. *Nat. Commun.* **2020**, *11*, No. 5483.
(40) Wang, Q.; Zhang, Q.; Luo, X.; Wang, J.; Zhu, R.; Liang, Q.; Zhang, L.; Yong, J. Z.; Wong, C. P. Y.; Eda, G.; Smet, J. H.; Wee, A. T. S. Optoelectronic Properties of a van der Waals Ws2 Monolayer/2d Perovskite Vertical Heterostructure. *ACS Appl. Mater. Interfaces* **2020**, *12*, 45235−45242.
(41) Zhang, Q.; Linardy, E.; Wang, X.; Eda, G. Excitonic Energy Transfer in Heterostructures of Quasi-2d Perovskite and Monolayer WS2. *ACS Nano* **2020**, *14*, 11482−11489.
(42) Chen, Y.; Liu, Z.; Li, J.; Cheng, X.; Ma, J.; Wang, H.; Li, D. Robust Interlayer Coupling in Two-dimensional Perovskite/monolayer Transition Metal Dichalcogenide Heterostructures. *ACS Nano* **2020**, *14*, 10258−10264.
(43) Yang, A.; Blancon, J.-C.; Jiang, W.; Zhang, H.; Wong, J.; Yan, E.; Lin, Y.-R.; Crochet, J.; Kanatzidis, M. G.; Jariwala, D.; Low, T.; Mohite, A. D.; Atwater, H. A. Giant Enhancement of effectivession in WS2-two-dimensional Perovskite Heterostructures. *Nano Lett.* **2019**, *19*, 4852−4860.
(44) Traore, B.; Pedesseau, L.; Assam, L.; Che, X.; Blancon, J.-C.; Tsai, H.; Nie, W.; Stoumpos, C. C.; Kanatzidis, M. G.; Tretiak, S.; Mohite, A. D.; Even, J.; Kepenekian, M.; Katan, C. Composite Nature of Layered Hybrid Perovskites: Assessment on Quantum and Dielectric Confinements and Band Alignment. *ACS Nano* **2018**, *12*, 3321−3332.
(45) Kang, J.; Tongay, S.; Zhou, J.; Li, J.; Wu, J. Band Offsets and Heterostructures of Two-dimensional Semiconductors. *Appl. Phys. Lett.* **2013**, *102*, No. 012111.
(46) Crowley, J. M.; Tahir-Kheli, J.; Goddard, W. A., III Resolution of the Band Gap Prediction Problem for Materials Design. *J. Phys. Chem. Lett.* **2016**, *7*, 1198−1203.
(47) Jadczak, J.; Kutrowska-Girzycka, J.; Kapuściński, P.; Huang, Y.; Wójs, A.; Bryja, z. Probing of Free and Localized Excitons and Trions in Atomically Thin Wse2, Ws2, Mose2 and Mos2 in Photoluminescence and Reflectivity Experiments. *Nanotechnology* **2017**, *28*, No. 395702.
(48) Feng, S.; Cong, C.; Konabe, S.; Zhang, J.; Shang, J.; Chen, Y.; Zou, C.; Cao, B.; Wu, L.; Peimyoo, N.; Zhang, B.; Yu, T. Engineering Valley Polarization of Monolayer Ws2: A Physical Doping Approach. *Small* **2019**, *15*, No. 1805503.
(49) Zhu, B.; Chen, X.; Cui, X. Exciton Binding Energy of Monolayer Ws 2. *Sci. Rep.* **2015**, *5*, No. 9218.
(50) Hong, X.; Ishihara, T.; Nurmikko, A. Dielectric Confinement Effect on Excitons in Pbi 4-based Layered Semiconductors. *Phys. Rev. B: Condens. Matter Mater. Phys.* **1992**, *45*, 6961.
(51) Straus, D. B.; Iotov, N.; Gau, M. R.; Zhao, Q.; Carroll, P. J.; Kagan, C. R. Longer Cations Increase Energetic Disorder in Excitonic 2d Hybrid Perovskites. *J. Phys. Chem. Lett.* **2019**, *10*, 1198−1205.
(52) Straus, D. B.; Hurtado Parra, S.; Iotov, N.; Zhao, Q.; Gau, M. R.; Carroll, P. J.; Kikkawa, J. M.; Kagan, C. R. Tailoring Hot Exciton Dynamics in 2d Hybrid Perovskites through Cation Modification. *ACS Nano* **2020**, *14*, 3621−3629.
(53) Kozawa, D.; Kumar, R.; Carvalho, A.; Amara, K. K.; Zhao, W.; Wang, S.; Toh, M.; Ribeiro, R. M.; Neto, A. H. C.; Matsuda, K.; Eda, G. Photocarrier Relaxation Pathway in Two-dimensional Semiconducting Transition Metal Dichalcogenides. *Nat. Commun.* **2014**, *5*, No. 4543.
(54) Feldstein, D.; Perea-Causin, R.; Wang, S.; Dyksik, M.; Watanabe, K.; Taniguchi, T.; Plochocka, P.; Malic, E. Microscopic Picture of Electron-phonon Interaction in Two-dimensional Halide Perovskites. *J. Phys. Chem. Lett.* **2020**, *11*, 9975−9982.
(55) Urban, J. M.; Chehade, G.; Dyksik, M.; Menahem, M.; Surrente, A.; Trippé-Allard, G.; Maude, D. K.; Garrot, D.; Yaffe, O.; Deleporte, E.; Plochocka, P.; Baranowski, M. Revealing Excitonic Phonon Coupling in (pea) 2 (ma) N- 1pb N I3 N+ 1 2d Layered Perovskites. *J. Phys. Chem. Lett.* **2020**, *11*, 5830−5835.
(56) Dyksik, M.; Duim, H.; Zhu, X.; Yang, Z.; Gen, M.; Kohama, Y.; Adjokatse, S.; Maude, D. K.; Loi, M. A.; Egger, D. A.; Baranowski, M.; Plochocka, P. Broad Tunability of Carrier Effective Masses in Two-

https://doi.org/10.1021/acsami.1c08377
ACS Appl. Mater. Interfaces 2021, 13, 33677−33684

dimensional Halide Perovskites. Acs. *Energy Lett.* **2020**, *5*, 3609−3616.
(57) Zeng, H.; Liu, G.-B.; Dai, J.; Yan, Y.; Zhu, B.; He, R.; Xie, L.; Xu, S.; Chen, X.; Yao, W.; Cui, X. Optical Signature of Symmetry Variations and Spin-valley Coupling in Atomically Thin Tungsten Dichalcogenides. *Sci. Rep.* **2013**, *3*, No. 1608.
(58) Baldo, M. A.; Thompson, M. E.; Forrest, S. R. High-efficiency Fluorescent Organic Light-emitting Devices Using a Phosphorescent Sensitizer. *Nature* **2000**, *403*, 750−753.
(59) Achermann, M.; Petruska, M. A.; Kos, S.; Smith, D. L.; Koleske, D. D.; Klimov, V. I. Energy-transfer Pumping of Semiconductor Nanocrystals Using an Epitaxial Quantum Well. *Nature* **2004**, *429*, 642−646.
(60) Zhou, J.; Lin, J.; Huang, X.; Zhou, Y.; Chen, Y.; Xia, J.; Wang, H.; Xie, Y.; Yu, H.; Lei, J.; Wu, D.; Liu, F.; Fu, Q.; Zeng, Q.; Hsu, C.-H.; Yang, C.; Lu, L.; Yu, T.; Shen, Z.; Lin, H.; Yakobson, B. I.; Liu, Q.; Suenaga, K.; Liu, G.; Liu, Z. A Library of Atomically Thin Metal Chalcogenides. *Nature* **2018**, *556*, 355−359.
(61) Kamminga, M. E.; Fang, H.-H.; Filip, M. R.; Giustino, F.; Baas, J.; Blake, G. R.; Loi, M. A.; Palstra, T. T. M. Confinement Effects in Low-dimensional Lead Iodide Perovskite Hybrids. *Chem. Mater.* **2016**, *28*, 4554−4562.
(62) Stradi, D.; Jelver, L.; Smidstrup, S.; Stokbro, K. Method for Determining Optimal Supercell Representation of Interfaces. *J. Phys.: Condens. Matter* **2017**, *29*, No. 185901.
(63) Aas, S.; Bulutay, C. Strain Dependence of Photoluminescence and Circular Dichroism in Transition Metal Dichalcogenides: Ak· P Analysis. *Opt. Express* **2018**, *26*, 28672−28681.
(64) Wang, S.; Gong, Z.; Li, G.; Du, Z.; Ma, J.; Shen, H.; Wang, J.; Li, W.; Ren, J.; Wen, X.; Li, D. The Strain Effects in 2d Hybrid Organic-inorganic Perovskite Microplates: Bandgap, Anisotropy and Stability. *Nanoscale* **2020**, *12*, 6644−6650.
(65) Tu, Q.; Spanopoulos, I.; Hao, S.; Wolverton, C.; Kanatzidis, M. G.; Shekhawat, G. S.; Dravid, V. P. Probing Strain-induced Band Gap Modulation in 2d Hybrid Organic-inorganic Perovskites. *Acs Energy Lett.* **2019**, *4*, 796−802.
(66) Kempt, R. Romankempt/hetbuilder: Zenodo Release, 2021-04, https://zenodo.org/record/4721346.
(67) Blum, V.; Gehrke, R.; Hanke, F.; Havu, P.; Havu, V.; Ren, X.; Reuter, K.; Scheffler, M. Ab Initio Molecular Simulations with Numeric Atom-centered Orbitals. *Comput. Phys. Commun.* **2009**, *180*, 2175−2196.
(68) Perdew, J. P.; Burke, K.; Ernzerhof, M. Generalized Gradient Approximation Made Simple. *Phys. Rev. Lett.* **1996**, *77*, 3865−3868.
(69) Tkatchenko, A.; Ambrosetti, A.; DiStasio, R. A. Interatomic Methods for the Dispersion Energy Derived from the Adiabatic Connection Fluctuation-dissipation Theorem. *J. Chem. Phys.* **2013**, *138*, No. 074106.
(70) Hermann, J.; Tkatchenko, A. Density Functional Model for van der Waals Interactions: Unifying Many-body Atomic Approaches with Nonlocal Functionals. *Phys. Rev. Lett.* **2020**, *124*, No. 146401.

https://doi.org/10.1021/acsami.1c08377
ACS Appl. Mater. Interfaces 2021, 13, 33677−33684